

blue is comments, red is edits

Comparison of Terrain Following and Cut Cell Grids with a Non-Hydrostatic Model

JAMES SHAW*

* C-grid finite volume (be specific in the abstract) ABSTRACT

Terrain following coordinates are widely used in operational models but, ~~more recently~~, the cut cell method has been proposed as an alternative that can more accurately represent the orography and associated atmospheric dynamics. Because the type of grid is usually chosen during model implementation, it is typically necessary to use different models in order to compare the accuracy of different grids. On the contrary, we use a single model to enable a like-for-like comparison of terrain following and cut cell grids. A series of standard two-dimensional tests using idealised terrain are performed: tracer advection in a prescribed horizontal velocity field, a test of a stably stratified atmosphere at rest, and orographically induced gravity waves. In addition, we formulate a new tracer advection test having a velocity field that is tangential to the ~~basic~~ terrain following coordinate surfaces. The results of the advection tests demonstrate that tracer accuracy depends upon alignment of the flow with the grid. In the gravity waves test, results on all grids are in good agreement with existing results from the literature. However, we find that the Lorenz computational mode is ~~manifested~~ excited as a vertical zig-zag in potential temperature only on the cut cell grid. Although errors do vary between grids, overall, a high degree of accuracy is obtained for all tests on all grids.

beautifully written abstract

1. Introduction

Representing orography accurately in numerical weather prediction systems is necessary to model downslope winds and local precipitation patterns. There are two main approaches to represent orography on a grid: terrain following layers and cut cells. Both methods align cells in vertical columns. Because most models are designed for a particular type of grid, existing studies of cut cells have compared results with terrain following grids using different models*. Instead, this study uses a single model to enable a like-for-like comparison between terrain following and cut cell grids.

With increasing model resolution, terrain can become steeper, making accurate calculation of the horizontal pressure gradient more difficult* (Gary 1973; Steppeler et al. 2002). Numerical errors in this calculation result in spurious winds and can cause numerical instability (Fast 2003; Webster et al. 2003). ~~Terrain following and~~ cut cell methods seek to reduce the error that is associated with steep orography.

With terrain following (TF) layers the terrain's influence decays with height so that the bottommost layers follow the underlying surface closely while the uppermost layers are flat. There are two main approaches to minimizing errors associated with TF layers. First, by smoothing the effects of terrain with height, the influence of the ter-

rain is reduced, hence errors in the calculated horizontal pressure gradient are also reduced aloft (Schär et al. 2002; Leuenberger et al. 2010; Klemp 2011). However, the error is not reduced at the ground where steep terrain remains unmodified.

Second, numerical errors can also be reduced by improving the accuracy in calculating the horizontal pressure gradient itself. TF layers are usually implemented using a coordinate transformation onto a rectangular computational domain, which introduces metric terms into the equations of motion. The techniques proposed by Klemp (2011) and Zängl (2012) both involve the calculation of the horizontal pressure gradient in the physical domain. ~~They found that, by avoiding the calculation of metric terms associated with the computational domain, numerical errors were reduced.~~ ***

Despite their associated numerical errors, TF layers are in widespread operational use (Steppeler et al. 2003). They are attractive because their rectangular structure is simple to process by computer, boundary layer resolution can be increased with variable spacing of vertical layers (Schär et al. 2002), and cell sizes remain almost constant (Jebens et al. 2011). ~~** the grid does not follow the terrain but instead~~ **

Cut cells is an alternative method in which cells that lie entirely below the terrain are removed, and those that intersect the surface are modified in shape so that they more closely fit the terrain. The resulting grid is orthogonal everywhere except near cells that have been cut. Hence, er-

*Corresponding author address: Department of Meteorology, University of Reading, Earley Gate, PO Box 243, Reading, RG6 6BB, UK.
E-mail: j.shaw@pgr.reading.ac.uk

*** I wouldn't say that it is the metric terms themselves that are the problem. You should always be able to create the same discretisation whether you are discretising in physical or computational space. Therefore instead you could say:

This gave them the flexibility to design more accurate horizontal pressure gradient discretizations using more appropriate stencils.

rors are still introduced when calculating the horizontal pressure gradient between cut and uncut cells.

The cut cell method can create some very small cells which reduce computational efficiency (Klein et al. 2009), and several approaches have been tried to alleviate the problem (Steppeler et al. 2002; Yamazaki and Satomura 2010; Jebens et al. 2011).

Several studies have found that cut cells produce more accurate results when compared to TF coordinates. Spurious winds seen in TF coordinates are not present and errors do not increase with steeper terrain (Good et al. 2014).

TODO: any other studies?

This study uses the nonhydrostatic model from Weller and Shahrokhi (2014) to enable a like-for-like comparison between terrain following and cut cell grids for idealised, two-dimensional test cases from the literature. Section 2 presents the formulation of the terrain following and cut cell grids used in the experiments that follow. Section 3 analyses the results from two tracer advection tests, a test of a stably stratified atmosphere at rest, and orographically induced gravity waves. Concluding remarks are made in section 4.

The term "sigma coordinates" is much more commonly used than BTF so I would use this description also. everybody knows what sigma coordinates are. very few know what BTF means

2. Grids

Here we describe the formulation of the terrain following grids and the method of cut cell grid construction. The techniques presented are used to define the grids for the experiments in the subsequent section.

Gal-Chen and Somerville (1975) proposed a basic terrain following (BTF) coordinate defined as

$$z = (H - h)(z^*/H) + h \quad (1)$$

where, in two dimensions, $z(x, z^*)$ is the height of the coordinate surface at level z^* , H is the height of the domain, and $h(x)$ is the height of the terrain surface. Using this coordinate, the terrain's influence decays linearly with height up to a given height or the but disappears only at the top of the domain. An example is shown in figure 1a.

The sigma coordinate transform of Phillips (1957) is equivalent to the BTF coordinate transform since they both decay linearly. However, since they decay with pressure rather than height, sigma coordinates also change with horizontal variations in pressure. This paragraph can be modified accordingly

The smooth level vertical (SLEVE) coordinate proposed by Schär et al. (2002) achieves a more regular TF grid in the middle and top of the domain than the BTF coordinate. The terrain height is split into large-scale and small-scale components, h_1 and h_2 , such that $h = h_1 + h_2$, with each component having a different exponential decay. The transformation is defined as

$$z = z^* + h_1 b_1 + h_2 b_2 \quad (2)$$

where the vertical decay functions are given by

$$b_i = \frac{\sinh((H/s_i)^n - (z^*/s_i)^n)}{\sinh(H/s_i)^n} \quad (3)$$

with s_1 and s_2 are the scale heights of large-scale and small-scale terrain respectively. The exponent n was introduced by Leuenberger et al. (2010) in order to increase cell thickness in the layers nearest the ground, allowing longer timesteps and permitting more accurate calculation of parameterised low-level heat and momentum fluxes. Leuenberger et al. (2010) found the exponent has an optimal value of $n = 1.35$. Choosing $n = 1$ gives the decay functions used by Schär et al. (2002). An example of the SLEVE grid can be seen in figure 1b.

Most implementations of terrain following layers use a coordinate system that makes the domain rectangular, but introduces metric terms into the equations of motion. Instead, the model employed in this study uses Cartesian coordinates and unstructured grids. By doing so, results from the same model can be compared between terrain following and cut cell grids without modifying the equation set or discretisation.

The OpenFOAM utility `snappyHexMesh` was used to create a grid that approximates the cut cell method. First, a custom utility was used to move points beneath the surface up to the surface creating small cells near mountain peaks. Second, the surface faces were taken from the BTF grid and `snappyHexMesh` was used to intersect the surface with the grid. The tool removes cells whose centres are below the surface. An example of the resulting grid is shown in figure 1c.

There are two details of grid construction which mean that resulting cut cell grids can differ slightly from a typical cut cell grid created using a shaving method, as described by Adcroft et al. (1997). First, when `snappyHexMesh` moves points along the surface according to its heuristics, some points are moved horizontally. Second, the utility does not create new points necessary for pentagonal cells.

3. Results

A series of standard, two-dimensional tests are performed over idealised orography. For each test, results on the BTF, SLEVE and cut cell grid are compared. The first test from Schär et al. (2002) advects a tracer in a horizontal velocity field. Second, a new tracer advection test is formulated employing a terrain following velocity field to challenge the advection scheme on more orthogonal grids. The third test solves the Euler equations for a stably stratified atmosphere at rest, following Klemp (2011). Finally, as specified by Schär et al. (2002), a test of orographically-induced gravity waves is performed.

We use a finite volume discretisation of the fully-compressible Euler equations described by Weller and

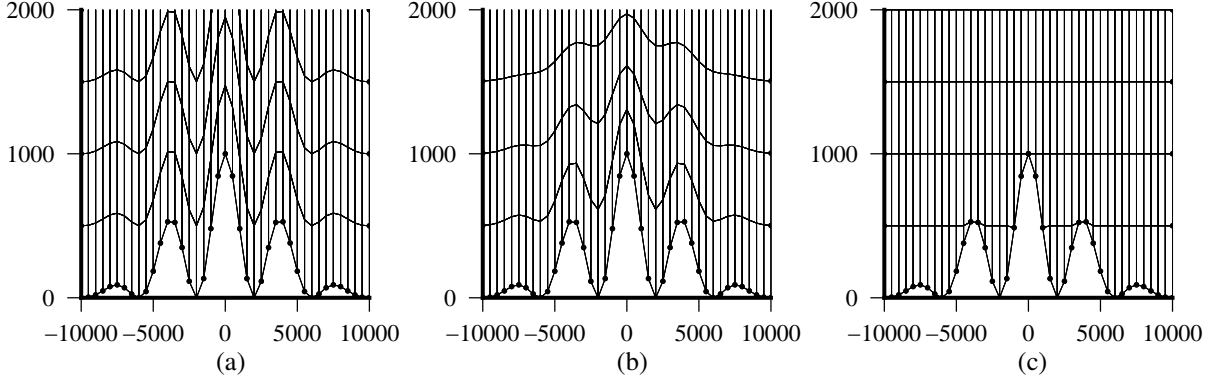


FIG. 1. Examples of (a) BTF, (b) SLEVE, and (c) a cut cell grid, all constructed with OpenFOAM. The two dimensional grids are 20 km wide and 2 km high. SLEVE parameters are specified in the resting atmosphere test in section 3c. The cut cell grid was created by intersecting the terrain surface with a regular grid as described in section 2.

Shahrokhi (2014). The model has a curl-free pressure gradient formulation, an upwind-biased cubic advection scheme, and uses a Lorenz staggering of thermodynamic variables. No explicit diffusion is used in any of the tests.

a. Horizontal advection

Following Schär et al. (2002), a tracer is transported above wave-shaped terrain by solving the advection equation for a prescribed horizontal wind. This test challenges the accuracy of the advection scheme in the presence of grid distortions.

The domain is 300 km wide and 25 km high, discretized onto a grid with $\Delta x = 1$ km and $\Delta z^* = 500$ m. The terrain is wave-shaped, specified by the surface height, h , such that

$$h(x) = h^* \cos^2(\alpha x) \quad (4a)$$

where

$$h^*(x) = \begin{cases} h_0 \cos^2(\beta x) & \text{if } |x| < a \\ 0 & \text{otherwise} \end{cases} \quad (4b)$$

where $a = 25$ km is the mountain half-width, $h_0 = 3$ km is the maximum mountain height, $\lambda = 8$ km is the wavelength, $\alpha = \pi/\lambda$ and $\beta = \pi/2a$. On the SLEVE grid, the large-scale component h_1 is given by $h_1(x) = h^*(x)/2$ and $s_1 = 15$ km is the large scale height, and $s_2 = 2.5$ km is the small scale height. The optimisation of SLEVE by Leuenberger et al. (2010) is not used, so the exponent $n = 1$.

The wind is entirely horizontal and is prescribed as

$$u(z) = u_0 \begin{cases} 1 & \text{if } z \geq z_2 \\ \sin^2\left(\frac{\pi}{2} \frac{z-z_1}{z_2-z_1}\right) & \text{if } z_1 < z < z_2 \\ 0 & \text{otherwise} \end{cases} \quad (5)$$

where $u_0 = 10 \text{ m s}^{-1}$, $z_1 = 4$ km and $z_2 = 5$ km. This results in a constant wind aloft, and zero flow at 4 km and below.

To ensure the discrete velocity field is non-divergent, velocities are prescribed at cell faces by summing the streamfunction at the centre of all face edges.

A tracer, ϕ , is positioned upstream above the height of the terrain. It has the shape

$$\phi(x, z) = \phi_0 \begin{cases} \cos^2\left(\frac{\pi r}{2}\right) & \text{if } r \leq 1 \\ 0 & \text{otherwise} \end{cases} \quad (6)$$

having radius, r , given by

$$r = \sqrt{\left(\frac{x-x_0}{A_x}\right)^2 + \left(\frac{z-z_0}{A_z}\right)^2} \quad (7)$$

where $A_x = 25$ km, $A_z = 3$ km are the horizontal and vertical half-widths respectively, and $\phi_0 = 1$ is the maximum magnitude of the anomaly. At $t = 0$ s, the anomaly is centred at $(x_0, z_0) = (-50 \text{ km}, 9 \text{ km})$ so that the anomaly is upwind of the mountain and well above the maximum terrain height of 3 km. Analytic solutions can be found by setting the anomaly centre such that $x_0 = ut$.

The flux form of the advection equation, $\partial\phi/\partial t + \nabla \cdot (u\phi) = 0$, is solved using an upwind-biased cubic advection scheme which is non-monotonic and not flux corrected. The time derivative is solved using a second order Runge-Kutta scheme. [Reiterate that the advection scheme and the time stepping scheme are defined in weller and shahrukhi](#)

Unlike Schär et al. (2002) who use periodic lateral boundaries, a fixed value of 0 is used at the inlet boundary and all other boundaries have zero gradient. Tests are integrated forward in time for 10000 s with a timestep of $\Delta t = 25$ s.

The test was executed on the BTF, SLEVE and cut cell grids, and on a regular grid with flat terrain. Tracer contours at $t = 0$ s, 5000 s and 10000 s are shown in Figure 2. The result from Schär et al. (2002) using a fourth-order centred scheme and sigma coordinates (2a) is compared with the upwind-biased cubic scheme on the BTF grid (2b), and cut cell grid (2c).

Tracer magnitude and shape are well-preserved on all grids, both above the mountain at $t = 5000$ s and past the mountain at $t = 10000$ s. Advection is most accurate on the cut cell grid (figure 2c) and regular grid (not shown). As found by Good et al. (2014), the result is the same on both grids. This is to be expected since the wind is zero in the region of the ground and flow aloft is aligned with the grids. On the BTF grid, the tracer is less distorted by the cubic upwind-biased scheme (figure 2b) compared to the fourth-order centred scheme from Schär et al. (2002) (figure 2a).

Minimum and maximum tracer values and ℓ^2 error norms on the BTF, SLEVE, cut cell and regular grids are summarised in table 1. The results of the cubic upwind-biased scheme on TF and regular grids are comparable with those for the fourth-order centred scheme from Schär et al. (2002). Error is largest on the BTF grid with $\ell^2 = 0.00767$ but significant reduced on the SLEVE grid with $\ell^2 = 0.00108$. The error is approximately halved by changing from the SLEVE grid to the cut cell grid.

The results of the tracer advection test show that, given an advection scheme of a sufficiently high order, distortions in the grid do not significantly distort the tracer.

you haven't shown this because you haven't shown results using a low order advection scheme
 b. Terrain following advection
 were the errors due to grid distortions or to the non alignment?

In the horizontal advection test, results were more accurate where the flow was aligned with the grid layers, and distortions in the BTF grid led to increased errors. We formulate a new tracer advection test in which the velocity field is everywhere tangential to the basic terrain following coordinate surfaces. In this new test, flow is aligned with the BTF grid layers. Misalignment on the SLEVE and cut cell grids is designed to challenge the advection scheme.

The spatial domain, mountain profile, initial tracer profile and discretisation are the same as those in the horizontal tracer advection test. The velocity field is defined using a streamfunction, Ψ , so that the continuous velocity field is non-divergent and follows the BTF coordinate surfaces given by equation 1 such that

$$\Psi(x, z) = u_0 H \frac{z - h}{H - h} \quad (8)$$

where $u_0 = 10 \text{ m s}^{-1}$, which is the horizontal wind speed where $h(x) = 0$. The horizontal and vertical components of velocity, u and w , are then given by

$$u = \frac{\partial \Psi}{\partial z} = u_0 \frac{H}{H - h}, \quad w = -\frac{\partial \Psi}{\partial x} = u_0 H \frac{dh}{dx} \frac{H - z}{(H - h)^2},$$

$$\frac{\partial h}{\partial x} = -h_0 [\beta \cos^2(\alpha x) \sin(2\beta x) + \alpha \cos^2(\beta x) \sin(2\alpha x)] \quad (9)$$

Unlike the horizontal advection test, flow extends from the top of the domain all the way to the ground. The discrete

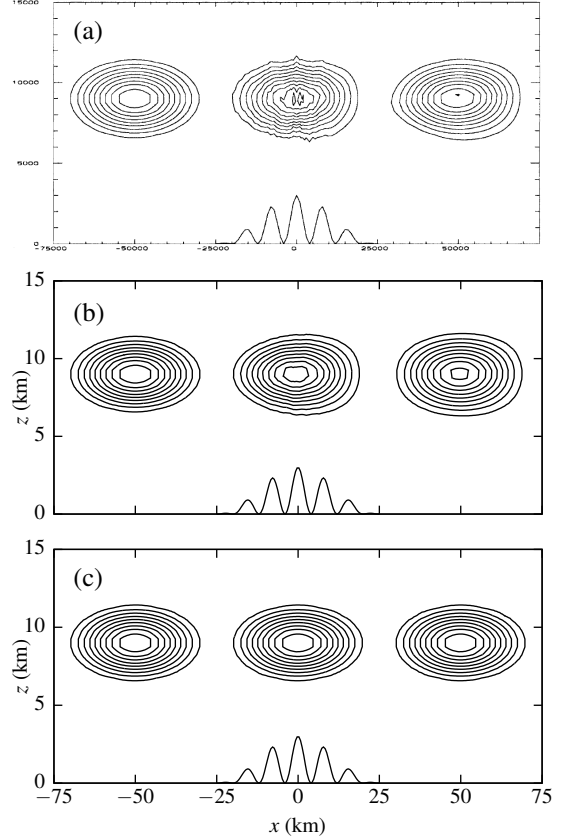


FIG. 2. Horizontally advected tracer contours at $t = 0$ s, 5000 s and 10000 s using (a) the fourth-order centred difference scheme with sigma coordinates from Schär et al. (2002), and the upwind-biased cubic scheme on (b) BTF grid, (c) cut cell grid. Contour intervals are every 0.1. The terrain profile is also shown immediately above the x axis.

velocity field is calculated using the streamfunction in the same way as the horizontal advection test.

At $t = 10000$ s the tracer has passed over the mountain. The horizontal position of the tracer centre can be calculated by integrating along the trajectory to find t , the time taken to pass from one side of the mountain to the other:

Say a little more about how you derived this equation

$$t = \frac{x}{u_0} - \frac{h_0}{16u_0H} \left[4x + \frac{\sin 2(\alpha + \beta)x}{\alpha + \beta} + \frac{\sin 2(\alpha - \beta)x}{\alpha - \beta} + 2 \left(\frac{\sin 2\alpha x}{\alpha} + \frac{\sin 2\beta x}{\beta} \right) \right] \quad (10)$$

Hence, we find that $x(t = 10000 \text{ s}) = 51577.4 \text{ m}$. Because the velocity field is non-divergent, the flow accelerates over mountain ridges and the tracer travels 1577.4 m further compared to advection in the horizontal velocity field. Tracer height is unchanged because advection is along the terrain following coordinate surface.

TABLE 1. Minimum and maximum tracer magnitudes and ℓ^2 error norms at $t = 10000$ s in the horizontal and terrain following tracer advection tests. In the horizontal advection test, results of the cubic upwind-biased scheme are compared with the fourth-order centred scheme from Schär et al. (2002).

	Horizontal advection					Terrain following advection		
	Schär 4th order		ℓ^2 error	Cubic upwind-biased		ℓ^2 error	Cubic upwind-biased	
	min	max		min	max		min	max
Analytic	0	0	1	0	1	0	0	1
BTF	-0.058	1.001	0.00767	-0.0433	0.928	0.00154	-0.0105	0.983
SLEVE	-0.002	0.984	0.00108	-0.0106	0.981	0.0122	-0.0273	0.864
Cut cell	—	—	0.000579	-0.00670	0.982	0.0136	-0.0297	0.850
No orography	-0.002	0.984	0.000577	-0.00670	0.982	—	—	—

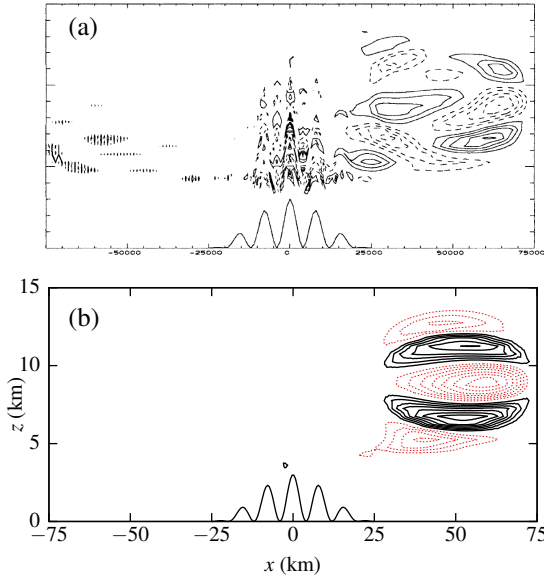


FIG. 3. Errors in horizontal tracer advection at $t = 10000$ s using (a) the fourth-order centred difference scheme with sigma coordinates from Schär et al. (2002), (b) the upwind-biased cubic scheme on a BTF grid. Contour intervals are every 0.01 with negative contours denoted by dashed lines.

ℓ^2 errors and tracer extrema for this test are compared with the horizontal advection results in table 1. In the terrain following velocity field, tracer accuracy is greatest on the BTF grid. Errors are about ten times larger on the SLEVE and cut cell grids compared to the BTF grid.

We conclude from this test that accuracy depends upon alignment of the flow with the grid, and accuracy is not significantly reduced by grid distortions. Error on the BTF grid is comparable with the error on the SLEVE grid in the horizontal advection test.

c. Resting atmosphere

An idealised terrain profile is defined along with a stably stratified atmosphere at rest in hydrostatic balance. The analytic solution is time-invariant, but numerical errors in calculating the horizontal pressure gradient can

give rise to spurious velocities which become more severe over steeper terrain (Klemp 2011).

The test setup follows the specification by Klemp (2011), but has a narrower domain that is 20 km wide and 20 km high in order to reduce simulation time, as used by Weller and Shahrokhi (2014). The grid resolution is $\Delta x = \Delta z^* = 500$ m as originally specified by Klemp (2011). All boundary conditions are no normal flow.

The wave-shaped mountain profile has a surface height, h , given by

$$h(x) = h_0 \exp\left(-\left(\frac{x}{a}\right)^2\right) \cos^2(\alpha x) \quad (11)$$

where $a = 5$ km is the mountain half-width, $h_0 = 1$ km is the maximum mountain height and $\lambda = 4$ km is the wavelength. For the optimised SLEVE grid, the large-scale component h_1 is specified as

$$h_1(x) = \frac{1}{2} h_0 \exp\left(-\left(\frac{x}{a}\right)^2\right) \quad (12)$$

and, following Leuenberger et al. (2010), $s_1 = 4$ km is the large scale height, $s_2 = 1$ km is the small scale height, and the optimal exponent value of $n = 1.35$ is used.

The initial thermodynamic conditions are in discrete hydrostatic balance, having a surface temperature of $\theta_0 = 288$ K and constant stability with Brunt-Väisälä frequency $N = 0.01$ s $^{-1}$ everywhere, except for a more stable layer of $N = 0.02$ s $^{-1}$ between $2 \text{ km} \leq z \leq 3 \text{ km}$. Unlike Klemp (2011), there is no eddy diffusion in the equation set.

The test was integrated forward by 5 hours on the BTF, SLEVE and cut cell grids, and a regular grid with flat terrain. Maximum vertical velocities are compared with the results from Klemp (2011) in figure 4 (note different vertical scales). In agreement with Klemp (2011), vertical velocities are larger on more distorted grids. However, magnitudes are smaller comparing results on the terrain following grids with those from Klemp (2011), with w reaching a maximum of ~ 0.35 m s $^{-1}$ on the BTF grid in our test compared with a maximum of ~ 10 m s $^{-1}$ found by Klemp (2011).

Unlike the result from Klemp (2011), the SLEVE grid does not significantly reduce vertical velocities compared

Less than 7 metres per second from Klemp figure 4

to the BTF grid. However, errors are three orders of magnitude smaller on the cut cell grid with vertical velocities of $\sim 1 \times 10^{-3} \text{ m s}^{-1}$. The smallest error of $\sim 1 \times 10^{-10} \text{ m s}^{-1}$ is found on the regular grid.

Good et al. (2014) found the maximum vertical velocity in their cut cell model was $1 \times 10^{-12} \text{ m s}^{-1}$, which is better than any result obtained using the model by Weller and Shahrokhi (2014). It is worth noting that, in the model used by Good et al. (2014), cell centres are in the centre of the uncut cell, resulting in the centre of some cut cells being below the ground (S.-J. Lock 2014, personal communication). This means that the grid is effectively regular when calculating horizontal and vertical gradients. This would ~~may~~ account for the very small velocities found by Good et al. (2014).

In summary, spurious velocities in the resting atmosphere test were similar on both terrain following grids, with ~~much~~ lower errors compared to those from Klemp (2011). The maximum vertical velocity was significantly decreased on the cut cell grid, so we conclude that non-orthogonality* is a significant cause of numerical error in this test.

* or lack of alignment of the grid with surfaces of constant gravitational potential are

d. Gravity waves

The test originally specified by Schär et al. (2002) prescribes flow over terrain with small-scale and large-scale undulations which induces propagating and evanescent gravity waves.

Following Melvin et al. (2010), the domain is 300 km wide and 30 km high. The mountain profile has the same form as equation 11. Tests are performed with mountain heights of $h_0 = 250 \text{ m}$ and $h_0 = 500 \text{ m}$. As in the resting atmosphere test, $a = 5 \text{ km}$ is the mountain half-width and $\lambda = 4 \text{ km}$ is the wavelength. On the optimised SLEVE grid, $s_1 = 5 \text{ km}$ is the large scale height, $s_2 = 2 \text{ km}$ is the small scale height and the optimal exponent value $n = 1.35$ is used.

The initial thermodynamic conditions have a surface temperature of $\theta_0 = 288 \text{ K}$ and constant stability with $N = 0.01 \text{ s}^{-1}$ everywhere. A constant horizontal wind $u = 10 \text{ m s}^{-1}$ is prescribed at the inlet boundary.

Sponge layers are added to the upper 10 km and leftmost 10 km at the inlet boundary to damp the reflection of waves. The term $\mu \rho \mathbf{u}$ is subtracted from the momentum equation ~~TODO: include the equation set in this paper, or cite weller-shahrokhi2014 here?~~ where the damping func-

tion μ is adapted from Melvin et al. (2010) such that

$$\mu(x, z) = \mu_{\text{upper}} + \mu_{\text{inlet}} \quad (13)$$

$$\mu_{\text{upper}}(z) = \begin{cases} \bar{\mu} \sin^2\left(\frac{\pi}{2} \frac{z - z_B}{H - z_B}\right) & \text{if } z \geq z_B \\ 0 & \text{otherwise} \end{cases} \quad (14)$$

$$\mu_{\text{inlet}}(x) = \begin{cases} \bar{\mu} \sin^2\left(\frac{\pi}{2} \frac{x_I - x}{x_I - x_0}\right) & \text{if } x < x_I \\ 0 & \text{otherwise} \end{cases} \quad (15)$$

where $\bar{\mu} = 1.2$ is the damping coefficient, $z_B = 20 \text{ km}$ is the bottom of the sponge layer, $H = 30 \text{ km}$ is the top of the domain, $x_0 = -150 \text{ km}$ is the leftmost limit of the domain and $x_I = -140 \text{ km}$ is the rightmost extent of the inlet sponge layer. The sponge layer is only active on faces whose normal is vertical so that it damps vertical momentum only. ~~TODO: is this true of the inlet sponge as well?~~

Note that, while the domain itself is 30 km in height, for the purposes of generating BTF and SLEVE grids, the domain height is set to 20 km because the sponge layer occupies the uppermost 10 km.

No normal flow is imposed at the top and bottom boundaries and the outlet is zero gradient. For Exner, hydrostatic balance is prescribed on all boundaries. The simulation is integrated forward by 5 hours with a timestep $\Delta t = 8 \text{ s}$.

Test results are compared between the BTF, SLEVE and cut cell grids. Vertical velocities on the BTF grid are shown in figure 5a, which have few visible differences from results on the SLEVE and cut cell grids (not shown). Vertical velocities on all grids are in agreement with the high resolution solution from Melvin et al. (2010), shown in figure 5b.

The initial thermal profile is subtracted from the potential temperature field at the end of the integration to reveal the structure of thermal anomalies. Once again, the results are similar on all three grids, and results are shown on the BTF and cut cell grids in figures 6a and 6c respectively. However, examining more closely the anomalies in the lee of the mountain, figure 6d shows that the bottom-most layer is anomalously warm and the layer above it is anomalously cold. This feature is not present on the BTF grid (figure 6b) or the SLEVE grid (not shown).

In a further test, the mountain height is doubled from 250 m to 500 m with all other parameter values unchanged. The same spurious anomaly in potential temperature is again present on the cut cell grid but its amplitude increases. Figure 7 shows vertical profiles of the Exner function of pressure and potential temperature in the lowest 1 km in the lee of the mountain at $x = 50 \text{ km}$. We find that the Exner function of pressure decreases linearly with height on all grids. The potential temperature increases linearly with height on the BTF and SLEVE grids. On the cut cell grid, the potential temperature anomalies seen in figure 6d appear as a zig-zag in figure 7.

The model by Weller and Shahrokhi (2014) has a Lorenz staggering of variables such that θ is stored at

Show Klemp figure 4 not figure 2

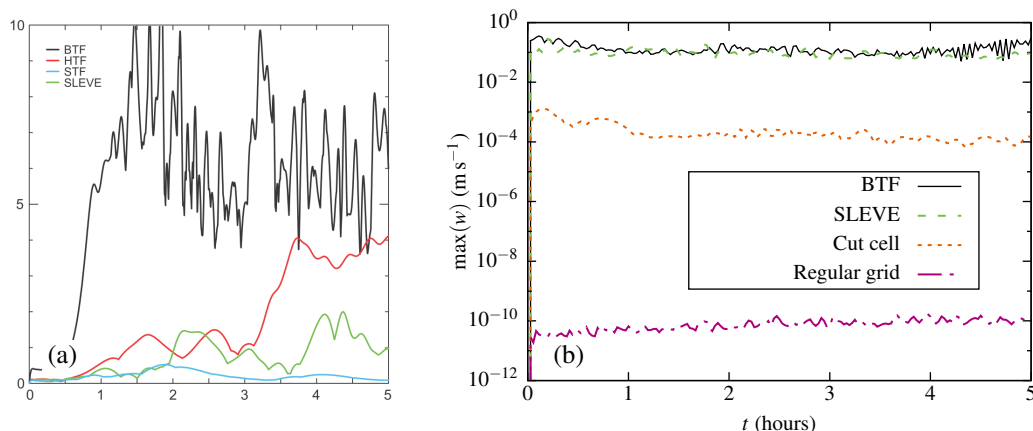


FIG. 4. Maximum spurious vertical velocity, w (m s⁻¹), in the resting atmosphere test with results on (a) BTF, SLEVE, Hybrid Terrain Following (HTF) and Smoothed Terrain Following (STF) coordinates from Klemp (2011), (b) BTF, SLEVE, cut cell and regular grids using the model from Weller and Shahrokhii (2014). Note that vertical scales differ.

cell centres and velocity at cell faces. The inaccuracies in potential temperature become invisible when calculating momentum because θ is interpolated onto cell faces, so discrete hydrostatic balance is maintained. This is a manifestation of the Lorenz computational mode, ~~which is a disadvantage of the Lorenz grid that has been widely discussed in the literature~~ (Arakawa and Konor 1996; Holdaway et al. 2013). In models that include moist processes, the Lorenz computational mode can disrupt clouds and generate spurious precipitation (Hollingsworth 1995).

To summarize, results of the gravity waves test on all grids are in good agreement with the reference solution from Melvin et al. (2010). The most prominent errors are found only on the cut cell grid, where the potential temperature errors near the ground ~~are maintained by~~ the Lorenz computational mode.

excite

4. Conclusions

We have presented a like-for-like comparison between terrain following and cut cell grids using a single model. Accuracy on the BTF, SLEVE and cut cell grids was evaluated in a series of two-dimensional tests.

Across all tests, a high degree of accuracy was achieved for all grids. Even on the highly-distorted BTF grid, which is often found to give poor results Schär et al. (2002); Klemp (2011); Good et al. (2014), errors were often small in the tests presented here. In the first two tests, tracers were advected ~~in~~ by horizontal and terrain following velocity fields. We found that the accuracy of the upwind-biased cubic advection scheme depended upon alignment of the flow with the grid. Spurious vertical velocities were small in the resting atmosphere test, reaching a maximum of ~ 0.35 m s⁻¹ on the BTF grid, compared to a maximum of ~ 10 m s⁻¹ found by Klemp (2011). In the gravity

* rather than on grid distortions

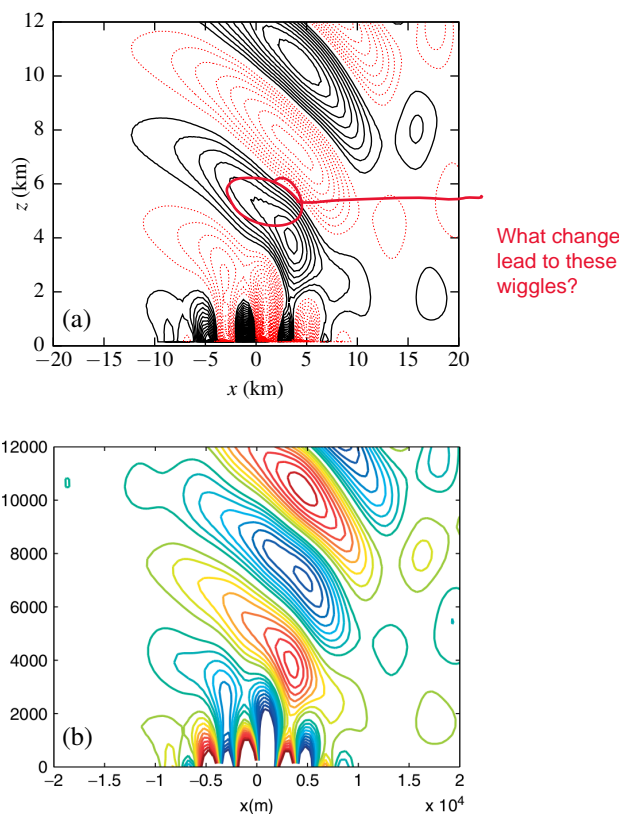


FIG. 5. Vertical cross section of vertical velocity contours in the gravity waves test after 5 hours with mountain height $h_0 = 250$ m on (a) the BTF grid compared with (b) the mass-conserving semi-implicit semi-Lagrangian solution from Melvin et al. (2010). Contours are every 5×10^{-2} m s⁻¹ with solid lines denoting ascent and dashed lines descent.

This sentence is a bit tricky to read

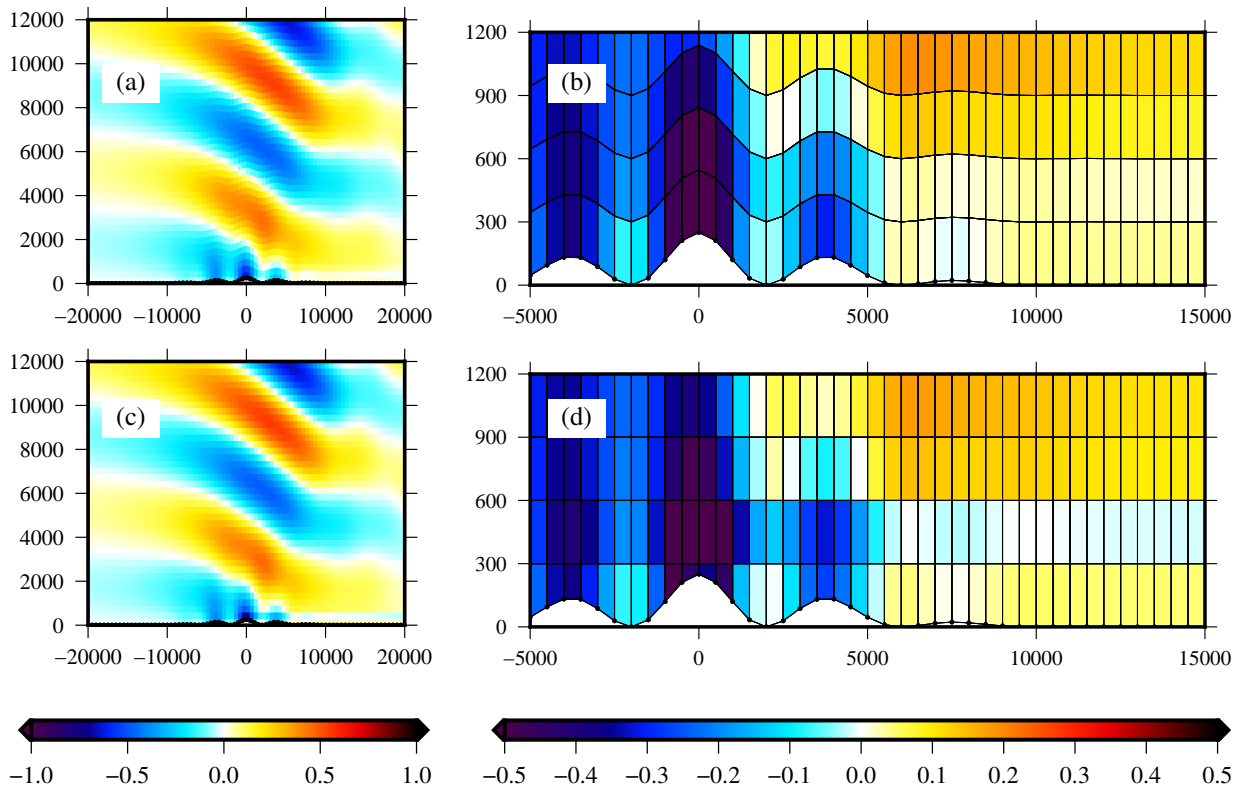


FIG. 6. Anomalies in potential temperature in the gravity waves test after 5 hours with a mountain height, $h_0 = 250$ m. The central domain in the lowest 12 km is shown on (a) the BTF grid, and (c) the cut cell grid. The four lowest layers of each grid are shown for (b) BTF, and (d) cut cell grids, using a narrower potential temperature scale. The results on the SLEVE grid (not shown) are qualitatively identical to results on the BTF grid.

waves test, vertical velocities were in good agreement with the reference solution from Melvin et al. (2010) across all grids.

Cut cell grids reduced errors in two of the four tests. First, in the horizontal advection test, tracer accuracy on the cut cell grid was almost as good as accuracy on a regular grid with no mountain. Second, in the resting atmosphere test, spurious vertical velocities were two orders of magnitude smaller on the cut cell grid compared with the terrain following grids.

Conversely, in the terrain following advection test, errors were large on the SLEVE and cut cell grids where velocities were misaligned with the grids. In the gravity waves test, the Lorenz computational mode was manifested as a zig-zag in potential temperature in the lowest layers in the lee of the mountain. This spurious error was excited only on the cut cell grid. This test motivates further work to formulate a Charney–Phillips staggering of variables on cut cell grids.

Acknowledgments. Start acknowledgments here.
TODO: John, Terry, S-J Lock. Assuming only Hilary is co-author...?

we should acknowledge our funders. We don't need to acknowledge S-J Lock. John and Terry should be listed as co authors unless they decline.

Weller is funded by NERC grant NE/H015698/1

References

- Adcroft, A., C. Hill, and J. Marshall, 1997: Representation of topography by shaved cells in a height coordinate ocean model. *Mon. Wea. Rev.*, **125**, 2293–2315.
- Arakawa, A., and C. S. Konor, 1996: Vertical differencing of the primitive equations based on the charney-phillips grid in hybrid σ – p vertical coordinates. *Mon. Wea. Rev.*, **124**, 511–528.
- Fast, J. D., 2003: Forecasts of valley circulations using the terrain-following and step-mountain vertical coordinates in the meso-eta model. *Wea. Forecasting*, **18**, 1192–1206.
- Gal-Chen, T., and R. C. Somerville, 1975: On the use of a coordinate transformation for the solution of the navier-stokes equations. *J. Comp. Phys.*, **17**, 209–228.
- Gary, J. M., 1973: Estimate of truncation error in transformed coordinate, primitive equation atmospheric models. *J. Atmos. Sci.*, **30**, 223–233.
- Good, B., A. Gadian, S.-J. Lock, and A. Ross, 2014: Performance of the cut-cell method of representing orography in idealized simulations. *Atmos. Sci. Lett.*, **15**, 44–49.
- Holdaway, D., J. Thuburn, and N. Wood, 2013: Comparison of lorenz and charney-phillips vertical discretisations for dynamics–boundary layer coupling. part ii: Transients. *Quart. J. Roy. Meteor. Soc.*, **139**, 1087–1098.

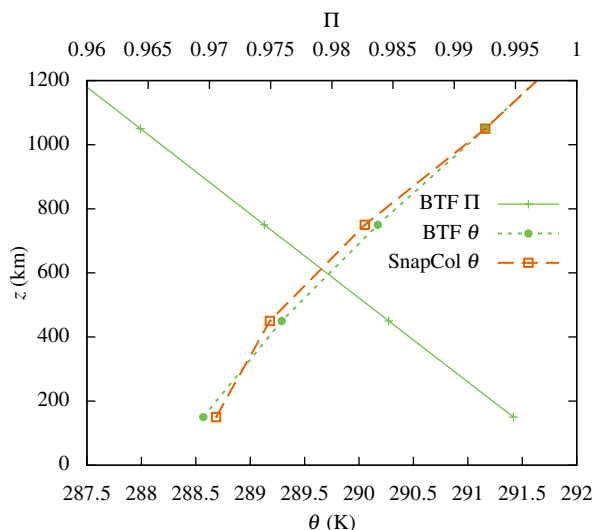


FIG. 7. Vertical profiles of the Exner function of pressure, Π , and potential temperature, θ , in the gravity waves test with a mountain height of $h_0 = 500$ m. Exner profile is visually identical on all grids for both mountain heights; for clarity, the Exner profile is only plotted for the BTF grid. The computational mode is manifested as a zig-zag in potential temperature on the cut cell grid which. Results on the SLEVE grid (not shown) are qualitatively the same as those on the BTF grid. The thermal profile with a lesser mountain height of $h_0 = 250$ m (not shown) exhibits a computational mode with smaller amplitude.

Hollingsworth, A., 1995: *A Spurious Mode in the 'Lorenz' Arrangement of f and T which Does Not Exist in the 'Charney–Phillips' Arrangement*. European Centre for Medium-Range Weather Forecasts.

Jebens, S., O. Knoth, and R. Weiner, 2011: Partially implicit peer methods for the compressible euler equations. *J. Comp. Phys.*, **230**, 4955–4974.

Klein, R., K. Bates, and N. Nikiforakis, 2009: Well-balanced compressible cut-cell simulation of atmospheric flow. *Philos. Trans. Roy. Soc. London*, **367**, 4559–4575.

Klemp, J. B., 2011: A terrain-following coordinate with smoothed coordinate surfaces. *Mon. Wea. Rev.*, **139**, 2163–2169.

Leuenberger, D., M. Koller, O. Fuhrer, and C. Schär, 2010: A generalization of the SLEVE vertical coordinate. *Mon. Wea. Rev.*, **138**, 3683–3689.

Melvin, T., M. Dubal, N. Wood, A. Staniforth, and M. Zerroukat, 2010: An inherently mass-conserving iterative semi-implicit semi-lagrangian discretization of the non-hydrostatic vertical-slice equations. *Quart. J. Roy. Meteor. Soc.*, **136**, 799–814.

Phillips, N. A., 1957: A coordinate system having some special advantages for numerical forecasting. *J. Meteor.*, **14**, 184–185.

Schär, C., D. Leuenberger, O. Fuhrer, D. Lüthi, and C. Girard, 2002: A new terrain-following vertical coordinate formulation for atmospheric prediction models. *Mon. Wea. Rev.*, **130**, 2459–2480.

Steppeler, J., H.-W. Bitzer, M. Minotte, and L. Bonaventura, 2002: Nonhydrostatic atmospheric modeling using a z -coordinate representation. *Mon. Wea. Rev.*, **130**, 2143–2149.

Steppeler, J., R. Hess, U. Schättler, and L. Bonaventura, 2003: Review of numerical methods for nonhydrostatic weather prediction models. *Meteor. Atmos. Phys.*, **82**, 287–301.

Webster, S., A. Brown, D. Cameron, and C. Jones, 2003: Improvements to the representation of orography in the met office unified model. *Quart. J. Roy. Meteor. Soc.*, **129**, 1989–2010.

Weller, H., and A. Shahrokhi, 2014: Curl free pressure gradients over orography in a solution of the fully compressible euler equations with implicit treatment of acoustic and gravity waves. *Mon. Wea. Rev.*, **142**, 4439–4457.

Yamazaki, H., and T. Satomura, 2010: Nonhydrostatic atmospheric modeling using a combined cartesian grid. *Mon. Wea. Rev.*, **138**, 3932–3945.

Zängl, G., 2012: Extending the numerical stability limit of terrain-following coordinate models over steep slopes. *Mon. Wea. Rev.*, **140**, 3722–3733.